

Constraining the slow-diffusion zone size and electron injection spectral index for the Geminga pulsar halo

Kun Fang*

*Key Laboratory of Particle Astrophysics,
Institute of High Energy Physics,
Chinese Academy of Sciences,
Beijing 100049, China*

(Dated: February 20, 2024)

Abstract

Measuring the electron diffusion coefficient is the most straightforward task in the study of gamma-ray pulsar halos. The updated measurements of the spatial morphology and spectrum of the Geminga halo by the High-Altitude Water Cherenkov (HAWC) experiment enable us to constrain parameters beyond the diffusion coefficient, including the size of the slow-diffusion zone and the electron injection spectrum from the pulsar wind nebulae (PWNe). Based on the two-zone diffusion model, we find that the slow-diffusion zone size (r_*) around Geminga is within the range of 30–70 pc. The lower boundary of this range is determined by the goodness of fit of the model to the one-dimensional morphology of the Geminga halo. The upper limit is derived from fitting the gamma-ray spectrum of the Geminga halo, along with the expectations for the power-law index of the injection spectrum based on simulations and PWNe observations, i.e., $p \gtrsim 1$. With r_* set at its lower limit of 30 pc, we obtain the maximum p permitted by the HAWC spectrum measurement, with an upper limit of 2.17 at a 3σ significance. Moreover, we find that when $r_* = 30$ pc and $p = 2.17$, the predicted positron spectrum generated by Geminga at Earth coincides with the AMS-02 measurement in the 50 – 500 GeV range.

* fangkun@ihep.ac.cn

I. INTRODUCTION

According to the standard evolution model, pulsar wind nebulae (PWNe) associated with middle-aged pulsars ($t \sim 100$ kyr) are typically in the bow-shock stage [1], during which they traverse the interstellar medium (ISM) while maintaining a compact size of $\lesssim 1$ pc. High-energy electrons and positrons¹ that escape from the PWNe and diffuse into the ISM generate gamma-ray halos around their respective pulsars via inverse Compton (IC) scattering of background photons. These phenomena are referred to as pulsar halos [2–5]. Since the morphology of pulsar halos traces the spatial distribution of their parent electrons, they serve as ideal indicators for investigating cosmic-ray propagation in localized regions of the Galaxy [6–10]. Furthermore, the gamma-ray spectrum of pulsar halos is determined by the energy spectrum of the escaped electrons rather than those remaining confined within the PWNe, thus providing unique insight into the process of electron escape from the PWNe [11, 12].

The diffusion coefficient inferred from the morphology of the identified pulsar halos is about two orders of magnitude smaller than the Galactic average [12–15], which also ensures that these halos are bright enough to be detected by current experiments. The slow-diffusion phenomenon around the pulsars has a crucial impact on interpreting issues such as the cosmic-ray positron excess [16–23] and the diffuse TeV gamma-ray excess [24–26]. To accurately address these issues, comprehension of the slow-diffusion mechanism is essential. This slow diffusion could be attributed to a turbulent environment generated by the host supernova remnants of the pulsars [7] or by the escaped electrons themselves [6, 27]. Alternatively, it may be explained by the projection effects under anisotropic diffusion without needing an additional turbulent magnetic field [8, 28, 29]. It has also been proposed that the steep profile of pulsar halos can be explained without the diffusion coefficient suppression as long as the relativistic correction is considered in the electron propagation equation [30]. However, this model provides poorer fits to the data when compared to the slow-diffusion scenario and requires an energy conversion efficiency significantly larger than 100% [31], which is unreasonable.

A definitive conclusion on the slow-diffusion mechanism remains elusive. Nonetheless, we can still investigate the physical parameters associated with pulsar halos phenomenologi-

¹ *Electrons* will denote both electrons and positrons hereafter if not specified.

cally. Recently, the High-Altitude Water Cherenkov (HAWC) experiment provided updated observations of a prototypical pulsar halo, namely the Geminga halo [32]. Compared to the initial work on the Geminga halo [13], the precision of the spatial morphology measurement has been significantly enhanced, and the gamma-ray flux has been accurately measured in distinct energy ranges. We will show that these improvements enable us to provide valuable constraints on the size of the slow-diffusion zone and the form of the PWN electron injection spectrum, thereby broadening our scope beyond simple diffusion coefficient measurements.

In this study, we ground our calculation in the two-zone diffusion model, where the slow-diffusion zone is confined to a specific vicinity around the pulsar. This phenomenological model could appropriately characterize the electron propagation associated with pulsar halos. In Sec. II, we present the calculation of the morphology and energy spectrum of the Geminga halo. In Sec. III, we fit the latest one-dimensional morphology measured by HAWC and give a lower limit for the slow-diffusion zone size using the goodness-of-fit test. In Sec. IV, we fit the gamma-ray energy spectrum of Geminga. The HAWC measurement shows a very hard spectrum in 2 – 20 TeV. We demonstrate that this feature can be interpreted by a reasonable electron injection spectrum under the two-zone diffusion model. We provide constraints on the index of the power-law term of the injection spectrum and also estimate the maximum slow-diffusion zone size. Based on these parameter constraints, Sec. V revisits the potential for Geminga to account for the cosmic-ray positron excess. Sec. VI is the conclusion.

II. TWO-ZONE DIFFUSION MODEL

The magnetic field turbulence downstream of the SNR shock could be significantly enhanced compared to the far upstream, resulting in a downstream diffusion coefficient two orders of magnitude smaller than the ISM [7, 33]. This suggests that the slow-diffusion environment can be understood if the pulsar remains within the downstream region of its corresponding SNR [7]. Among the observed pulsar halos, the pulsar associated with the Monogem halo indeed resides within the downstream region of its corresponding SNR, which has been strongly supported by pulsar scintillation observations [34]. Given the scale of SNRs, the slow-diffusion zone around pulsars may span several tens of parsecs.

Alternatively, if the slow diffusion is attributed to the escaped electrons from PWNe

amplifying the surrounding magnetic turbulence via streaming instability, the diffusion coefficient could only be significantly reduced in the vicinity of pulsars as the growth rate of turbulence is directly proportional to the electron number density gradient [6]. Therefore, a two-zone diffusion model with a slow-diffusion zone spanning several tens of parsecs is a plausible approximation. The current paper does not discuss the scenario of interpreting pulsar halos with anisotropic diffusion.

High-energy electrons are accelerated by PWNe and subsequently released into the ISM. The electron propagation in the ISM could be described by the diffusion-loss equation as

$$\frac{\partial n(E_e, \mathbf{r}, t)}{\partial t} = \nabla \cdot [D(E_e, \mathbf{r}) \nabla n(E_e, \mathbf{r}, t)] + \frac{\partial [b(E_e) n(E_e, \mathbf{r}, t)]}{\partial E_e} + Q(E_e, \mathbf{r}, t), \quad (1)$$

where $n \equiv dN/dE_e$ is the differential electron number density, and E_e is the electron energy. The diffusion coefficient in the two-zone diffusion model takes the form of

$$D(E_e, \mathbf{r}) = \begin{cases} D_{100}(E_e/100 \text{ TeV})^\delta, & |\mathbf{r} - \mathbf{r}_p| \leq r_* \\ D_{100,\text{ism}}(E_e/100 \text{ TeV})^{\delta_{\text{ism}}}, & |\mathbf{r} - \mathbf{r}_p| > r_* \end{cases}, \quad (2)$$

where \mathbf{r}_p is the location of the pulsar, r_* is the size of the slow-diffusion zone, D_{100} and δ are diffusion parameters for the slow-diffusion zone, and $D_{100,\text{ism}}$ and δ_{ism} are those for the typical ISM. Considering the energy range of the HAWC measurement, we set the reference energy for the diffusion coefficient at 100 TeV. This ensures that D_{100} is minimally affected by the selection of δ . We adopt $D_{100,\text{ism}} = 3.4 \times 10^{30} \text{ cm s}^{-1}$ and $\delta_{\text{ism}} = 0.38$ as inferred from the cosmic-ray boron-to-carbon ratio [35].

The second term on the right-hand side of Eq. (1) is the energy-loss term, where $b(E_e) \equiv |dE_e/dt|$ is the electron energy-loss rate. We take the magnetic field strength of $B = 3 \mu\text{G}$ for the synchrotron loss rate. For the IC scattering, we adopt the seed photon field given in Ref. [13] and the parametrization method given in Ref. [36] to calculate the energy-loss rate.

The third term on the right-hand side of Eq. (1) is the source term. Assuming the time profile of the source function follows the pulsar spin-down luminosity, it takes the form of

$$Q(E_e, \mathbf{r}, t) = \begin{cases} q(E_e) [(t_p + t_{\text{sd}})/(t + t_{\text{sd}})]^2 \delta(\mathbf{r} - \mathbf{r}_p), & t \geq 0 \\ 0, & t < 0 \end{cases}, \quad (3)$$

where $q(E_e)$ is the current electron injection spectrum, t_p is the characteristic age of the pulsar, t_{sd} is the pulsar spin-down timescale, and $t = 0$ corresponds to the birth time of

the pulsar. The characteristic age of Geminga is $t_p = 342$ kyr as given by the Australia Telescope Nation Facility (ATNF) pulsar catalog [37], and t_{sd} is set to be 10 kyr.

The injection energy spectrum is assumed to be a power law with a super-exponential cutoff as

$$q(E_e) \propto E_e^{-p} \exp \left[- \left(\frac{E_e}{E_c} \right)^2 \right], \quad (4)$$

where the form of the cutoff term is suggested by the mechanism of the relativistic shock acceleration [38].

We numerically solve Eq. (1) using the finite volume method [17]. A semianalytical method is also applicable for two-zone diffusion [39]. We integrate the resulting electron number density n over the line of sight from Earth to the vicinity of the pulsar to obtain the electron surface density. This allows us to derive the one-dimensional gamma-ray morphology of the halo, $s(\theta, E_\gamma)$, using the standard calculation of IC scattering [40], where θ is the angle away from the pulsar. The gamma-ray spectrum within an arbitrary angular radius around the pulsar is then calculated by

$$\frac{dF}{dE_\gamma}(\theta < \theta_0, E_\gamma) = \int_0^{\theta_0} s(\theta, E_\gamma) 2\pi\theta d\theta. \quad (5)$$

The distance of the Geminga pulsar to the Earth takes 250 pc as measured by trigonometric parallax [41].

III. LOWER LIMIT OF THE SLOW-DIFFUSION ZONE SIZE

The one-dimensional gamma-ray morphology of the Geminga halo provided by HAWC, also known as the surface brightness profile (SBP), exhibits a median energy of ≈ 20 TeV [32]. This corresponds to a parent electron energy of ≈ 100 TeV [13]. Therefore, the shape of the SBP is predominantly determined by the diffusion coefficient at 100 TeV and is minimally influenced by parameters describing energy dependence, such as δ or p . In the fitting process of this section, we consider D_{100} and the normalization as free parameters. The values of δ and p remain fixed as in the initial HAWC paper [13], and we find that variations in these parameters have negligible impact on the fitting results. To compare with the HAWC data, we also convolve a point spread function with a 68% containment radius of 0.3° on the model.

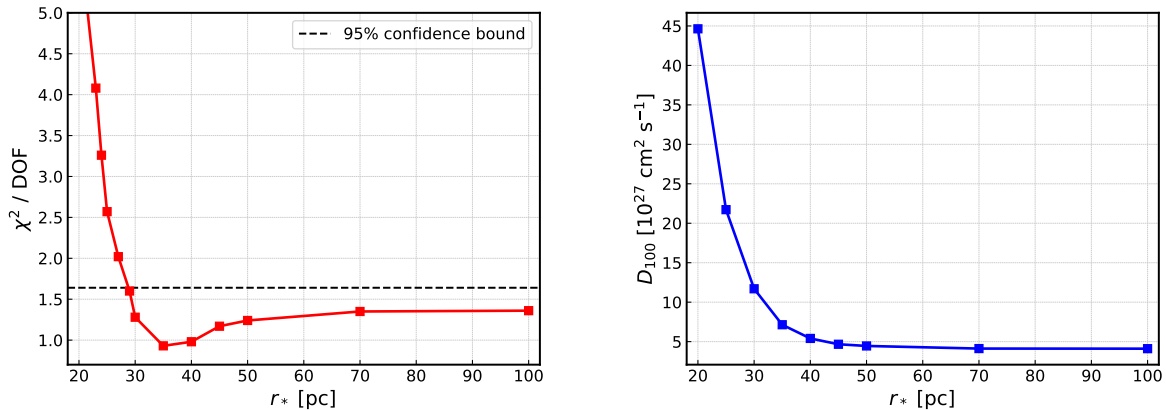


FIG. 1. The fitting results for the Geminga halo SBP measured by HAWC assuming different slow-diffusion zone sizes (r_*). The left panel shows the minimum reduced chi-square statistic with 16 d.o.f. The right panel depicts the corresponding diffusion coefficient of the slow-diffusion zone at the energy of 100 TeV.

The SBP centered on Geminga provided by HAWC includes contributions from both the Geminga and Monogem halos. The component of the Monogem halo is determined using the SBP measurement center on Monogem, where only the data within a radius of 3° is considered to avoid significant influence from the Geminga halo at larger angles. The Monogem halo is characterized using a one-zone diffusion model, yielding $D_{100} = 4.6 \times 10^{27} \text{ cm s}^{-1}$. We fix the Monogem halo component in the following fitting process.

We assume varying sizes for the slow-diffusion zone and fit these models to the SBP data centered on Geminga. The minimum reduced chi-square statistic χ^2 for each r_* is illustrated in the left panel of Fig. 1. With 16 degrees of freedom (d.o.f.), the 95% confidence bound for the reduced χ^2 is 1.64, as marked by the dashed line in the figure. It can be seen that models with $r_* \lesssim 30$ pc are excluded at the 95% confidence level by the chi-square test. The chi-square statistic is minimized at ≈ 1.0 when $r_* = 35$ pc. Beyond $r_* \gtrsim 50$ pc, there is no significant change in the goodness of fit. The corresponding D_{100} for each r_* is depicted in the right panel of Fig. 1. When $r_* \gtrsim 40$ pc, the best-fit D_{100} tends to be $\approx 4.5 \times 10^{27} \text{ cm}^2 \text{ s}^{-1}$, consistent with that given by the HAWC paper. For models with $r_* < 40$ pc, a larger D_{100} is required to widen the SBP to match the data.

Figure 2 provides an intuitive explanation for excluding models with a small r_* . In the two-zone diffusion model, electrons disperse rapidly once they leave the slow-diffusion zone,

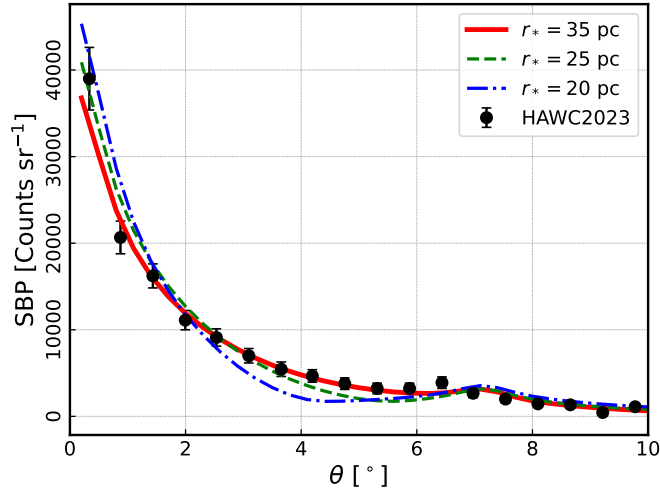


FIG. 2. Best-fit models for the SBP centered on Geminga under different assumptions of the slow-diffusion zone size. This figure serves to explain the exclusion of models with a small r_* intuitively. The case of $r_* = 35$ pc provides the best fit among all models, with $\chi^2/\text{d.o.f.} = 0.93$, as shown in the left panel of Fig. 1.

resulting in a significant flux reduction in the fast-diffusion zone compared to the slow-diffusion zone. The flux of the fast-diffusion zone is so low that it is difficult to distinguish them from the background. As a result, the SBP of the pulsar halo under two-zone diffusion appears to be more contracted if r_* is smaller. As shown in the right panel of Fig. 1, the best-fit value of D_{100} determined by the fitting process increases in an attempt to compensate for the reduction in the halo extent caused by the decrease in r_* . If r_* is too small, a significant reduction in flux will occur at a location too close to the pulsar. For instance, in the case of $r_* = 20$ pc depicted in Fig. 2, the model significantly underestimates the data in the angular range of $\approx 2^\circ$ to 6° due to the transition from the slow- to fast-diffusion zone. This results in a very poor goodness of fit that cannot be rectified by assuming a larger D_{100} .

On the other hand, the current SBP measurement does not constrain the upper limit of r_* . For Geminga, an angular distance of 10° corresponds to a transverse spatial distance of ≈ 45 pc. This means that when r_* exceeds 45 pc, the variation in SBP within 10° predicted by different models is insignificant. However, as we will show in the next section, the gamma-ray energy spectrum could enable us to estimate the upper limit of r_* .

Although HAWC also provides the preliminary SBP centered on Monogem, since the

Monogem halo is significantly dimmer than the Geminga halo, the SBP is heavily influenced by the Geminga halo at large angles. The Geminga halo may display asymmetry in its morphology [42], but in the absence of two-dimensional data, we cannot estimate the contribution of the Geminga halo to this SBP accurately. Therefore, we do not investigate the slow-diffusion zone size corresponding to the Monogem halo in this study.

IV. CONSTRAINTS OF GAMMA-RAY SPECTRUM ON PARAMETERS

The HAWC spectrum measurement of the Geminga halo ranging from $\approx 1 - 100$ TeV indicates that the electron injection spectrum is consistent with the form presented in Eq. (4), with $E_c \approx 100$ TeV. Nevertheless, the gamma-ray spectrum from 2 TeV to 20 TeV exhibits a hard nature, indicating the necessity for a hard power-law term in the injection spectrum. However, under one-zone diffusion, even though a very hard injection spectrum of $p \approx 1$ is assumed, the model still does not fit the observed gamma-ray spectrum well [32].

Assuming the one-zone diffusion model with $D_{100} = 5 \times 10^{27} \text{ cm}^2 \text{ s}^{-1}$ and $\delta = 1/3$, as used in the HAWC work, the gamma-ray flux within 10° around the pulsar constitutes $\approx 98\%$ of the total angle-integrated spectrum. Consequently, the spectral measurement provided by HAWC approximately represents the integrated gamma-ray spectrum within $\theta = 10^\circ$.

The integrated gamma-ray spectrum within a specific angle θ_0 is determined not only by the electron injection spectrum but also by δ and r_* , as illustrated in Fig. 3, where $\theta_0 = 10^\circ$. Given that D_{100} is constrained by the SBP data, a smaller δ corresponds to faster diffusion of low-energy electrons, making them more likely to escape from θ_0 and consequently yielding a harder gamma-ray spectrum. Moreover, within the energy range of interest, the characteristic diffusion distance ($\sim \sqrt{D\tau}$, where τ is the smaller one between the electron cooling time and the pulsar age) of low-energy electrons is larger than that of high-energy electrons. This implies that a smaller r_* results in a higher proportion of low-energy electrons escaping from θ_0 , thereby producing a harder gamma-ray spectrum. As can be seen from Fig. 3, the impact of r_* on the spectral shape is significant. Therefore, under the two-zone diffusion model, a very hard injection spectrum might not be necessary. This point has also been demonstrated in our previous studies [10, 12].

The analysis in Sec. III indicates that $r_* = 30$ pc may serve as the lower limit for the slow-diffusion size, and we typically regard $\delta = 0$ as the lower limit for the energy index of

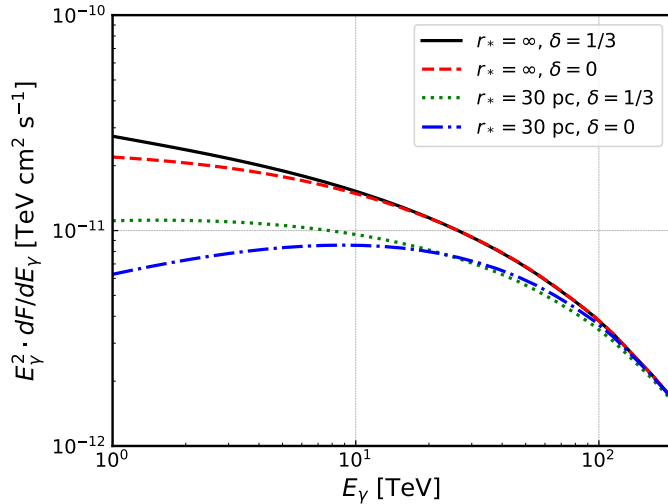


FIG. 3. This figure illustrates the impact of the energy index of the diffusion coefficient (δ) and the size of the slow-diffusion zone (r_*) on the angle-integrated gamma-ray spectrum within 10° around the Geminga pulsar. The electron injection spectrum is assumed to be a power law with $p = 2.2$. The gamma-ray spectral softening at high energies is due to the Klein-Nishina effect.

the diffusion coefficient. Such energy-independent diffusion of electrons can occur if their transport is governed by the field-line random walk within the ISM turbulence [43], or when the electrons are scattered by fast-mode turbulence in a regime where the damping of the turbulence cascade is collisionless [44]. With this set of parameters, we explore the maximum permissible injection spectral index derived from the observation. We fit the integrated gamma-ray spectrum obtained from the model within $\theta = 10^\circ$ to the spectral measurements of the Geminga halo by HAWC (including the flux upper limits with 95% confidence), with p , E_c , and the normalization as free parameters. We impose constraints on p using the likelihood ratio test. The likelihood ratio is defined as $\lambda = -2 \ln [L(p_0)/L(p)]$, where $L(p)$ is the global maximum likelihood, and $L(p_0)$ is the local maximum likelihood when the spectral index is fixed at p_0 . According to Wilks' theorem, λ follows the chi-square distribution with one degree of freedom. When λ equals 4 and 9, we can respectively determine the 2σ and 3σ confidence bounds for p .

The maximum likelihood p we obtained is 1.18, and the upper limits at 2σ and 3σ confidence levels are 1.85 and 2.17, respectively. The fitting effects of these three scenarios on the data are illustrated in Fig. 4. It can be seen that when p is larger, the model tends to

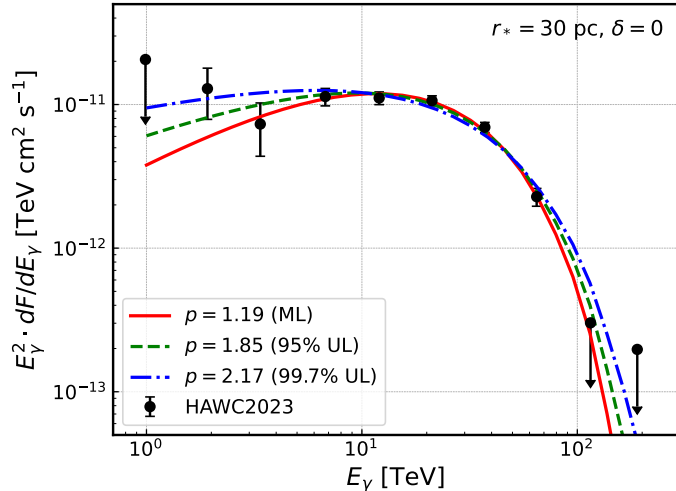


FIG. 4. Fitting results of the Geminga halo gamma-ray spectrum by the two-zone diffusion model. The model represents the angle-integrated spectrum within 10° around the pulsar, adopting the smallest r_* and δ to achieve the largest possible injection spectral index p . The three models in the figure include the maximum likelihood model and models using the 2σ and 3σ confidence upper limits of p . The best-fit E_c for these scenarios are all around 100 TeV.

TABLE I. Power-law index of the electron injection spectrum (p) resulted from the fitting of the HAWC gamma-ray spectrum, under the assumption that the slow-diffusion zone size is 30 pc. Values lower than expectations, namely $p < 1$, are denoted in italics.

δ	p		
	Maximum likelihood	2σ upper limit	3σ upper limit
0	1.19	1.85	2.17
1/3	<i>0.81</i>	1.36	1.82
1/2	<i>0.59</i>	1.17	1.65

overestimate the flux at low- and high-energy ranges while underestimating the flux at the intermediate-energy range. The best-fit E_c in different scenarios are all around 100 TeV. For larger δ values, such as $\delta = 1/3$ or $\delta = 1/2$, as predicted by Komolgorov's or Kraichnan's theory, the resulting injection spectral index is correspondingly smaller. We have reiterated the fitting procedure and summarized the results in Table I.

TABLE II. 3σ confidence upper limits of the power-law index of the electron injection spectrum (p) resulted from fitting the HAWC gamma-ray spectrum, assuming $\delta = 0$. Values lower than expectations, namely $p < 1$, are denoted in italics.

r_* [pc]	30	40	50	60	70
UL for p	2.17	1.60	1.32	1.03	<i>0.87</i>

On the other hand, we fit the spectral data under the assumption of varying r_* values while maintaining $\delta = 0$. The derived 3σ confidence upper limits of p from these fits are summarized in Table II, indicating a decrease in the upper limit of p as r_* increases. Numerical simulations suggest that the spectral index of electrons within a bow-shock PWN could approach 1 at the colliding flow between the stellar-wind termination shock and the bow shock [45]. However, existing theories or observations do not support spectral indices to be smaller. Moreover, the x-ray PWN of Geminga exhibits two components with distinct spectral indices, with the harder and softer components corresponding to $p = 1.08$ and 2.26 , respectively [46]. As discussed in Ref. [11], these components may indicate two disparate modes of electron escape, suggesting that the total injection spectrum could be a composite of both components. Consequently, for the Geminga halo, an injection spectral index of 1 can be regarded as the lower limit. This allows us to estimate the upper limit of r_* . At $r_* = 70$ pc, the upper limit of p falls below 1, suggesting that models with $r_* \geq 70$ pc are disfavored. Combined with the lower limit obtained in Sec. III, we are able to provide a comprehensive constraint on the slow-diffusion zone size, which lies between 30 and 70 pc.

In comparison, Ref. [23] estimates r_* for the Geminga halo to be 20 – 50 pc, but these constraints are not derived from a direct fit to the data. Using the new data from HAWC, our analysis demonstrates that scenarios with $r_* < 30$ pc can be excluded with high significance, providing a more stringent lower limit for r_* than Ref. [23]. The upper limit of 50 pc suggested by Ref. [23] is derived from a general estimate for this type of source [16], whereas our upper limit is based on observational constraints specific to the Geminga halo. Additionally, while Ref. [23] argues that the power index p of the electron injection spectrum is around 2.0, our findings suggest that the uncertainty in r_* necessitates a range of possible values for p , resulting in a more comprehensive conclusion.

Recently, the x-ray observation by eROSITA provides an upper limit of $1.4 \mu\text{G}$ for the ISM

magnetic field within 1° around the Geminga pulsar [47]. This is lower than the $3 \mu\text{G}$ adopted in the initial HAWC study and our above calculations. Thus, we also consider a scenario with $B = 1 \mu\text{G}$, where the synchrotron energy-loss rate for electrons is significantly reduced. This change notably affects the lifetime of higher-energy electrons, thereby influencing the estimation of the cutoff term in the electron injection spectrum. When B shifts from $3 \mu\text{G}$ to $1 \mu\text{G}$ in the case of $r_* = 30 \text{ pc}$ and $\delta = 0$, the best-fit E_c varies from 94 TeV to 83 TeV. However, this adjustment in magnetic field strength has a negligible effect on p , with its 3σ confidence upper limit merely changing from 2.17 to 2.19, leaving our conclusion unaffected.

V. IMPLICATION ON THE POSITRON EXCESS

The positron excess is one of the most intriguing phenomena in cosmic-ray studies. As measured by space experiments [48–50], the positron spectrum above several tens of GeV significantly exceeds the predicted secondary positron flux produced by cosmic-ray nuclei spallation during Galactic propagation. Among astrophysical accelerators, pulsars (or their PWNe) are the most plausible sources of this excess [51–53], given their capacity to generate high-energy electron/positron pairs.

The positron spectrum measured by AMS-02 reveals a high-energy cutoff at $\approx 800 \text{ GeV}$ with a significance of 4.7σ [54, 55]. As discussed in our previous studies, this cutoff is likely attributed to the cooling effect of the positrons generated by a dominant source rather than the superposition of multiple sources [20]. This is due to the fact that pulsars or PWNe are unlikely to share a common acceleration limit at $\sim 1 \text{ TeV}$. Among observed pulsars, the most plausible dominant sources of the positron excess are Geminga, Monogem, and PSR B1055-52 [20, 56, 57], all of which are nearby and middle-aged pulsars.

Within the framework of the two-zone diffusion model, the contribution of nearby pulsars to the positron spectrum at Earth is primarily affected by parameters such as the diffusion coefficient, the slow-diffusion zone size, and the positron injection spectrum. We use parameters determined from fitting the HAWC data (as detailed in Secs. III and IV) to predict the contribution of Geminga to the positron spectrum at Earth. As shown in Fig. 2 of Ref. [20], the positron spectrum produced by Geminga, under assumptions of $r_* = 50 \text{ pc}$ and $p = 1.8$, is too hard compared to the AMS-02 measurement. Reducing r_* or increasing p can yield a softer positron spectrum. Intriguingly, as indicated in Table II, an inverse correlation exists

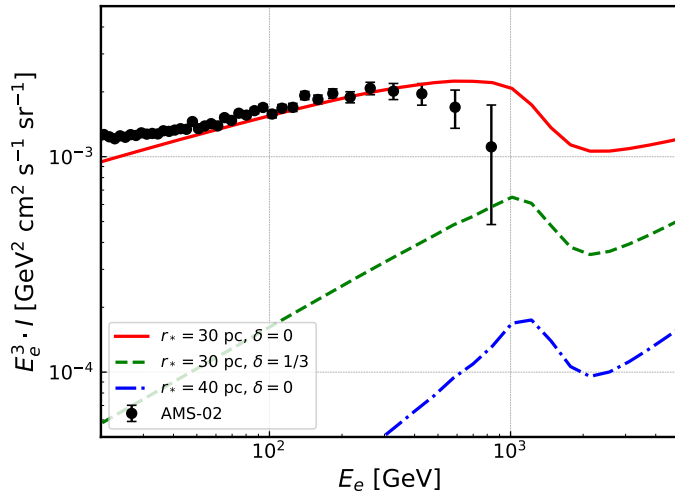


FIG. 5. The predicted positron spectrum from Geminga under different assumptions of r_* and δ , along with the corresponding D_0 , p , and normalization determined by the fits in Secs. III and IV, where p is adopted as the 3σ upper limits as presented in Tables I and II. The scenario with $r_* = 30$ pc and $\delta = 0$ provides the most optimistic prediction to the AMS-02 measurements among all the models consistent with the HAWC measurements of the Geminga halo.

between the required p and r_* when interpreting the gamma-ray spectrum of the Geminga halo. Consequently, by setting r_* to its lower limit of 30 pc, we can achieve the softest possible positron spectrum at Earth. Furthermore, a smaller δ corresponds to faster diffusion of low-energy positrons, enabling more low-energy positrons to reach Earth and further soften the spectrum.

As an optimistic estimate, we adopt $r_* = 30$ pc and $\delta = 0$, along with the upper limit of the injection spectrum index $p = 2.17$ and the corresponding best-fit normalization derived in Sec. IV. The predicted positron energy spectrum, $I(E_e) = n(E_e)c/4\pi$, depicted by the red solid line in Fig. 5, is consistent with the measurements of both absolute flux and spectral shape below ≈ 500 GeV. Below ≈ 50 GeV, the secondary component may dominate the positron spectrum. However, the predicted spectral cutoff occurs at a higher energy than observed. One possible explanation is that the positrons traverse regions with higher magnetic field strength than assumed, resulting in a spectral cutoff at lower energies. Alternatively, an older pulsar, such as PSR B1055-52, could be the main contributor to the high-energy positrons instead of Geminga. Figure 5 also shows two additional scenarios with a larger r_*

or a larger δ , where p is set as the corresponding 3σ confidence limits presented in Tables I and II. Under these conditions, the positron flux produced by Geminga is insufficient to interpret the observation.

It should be noted that the calculations above are based on extrapolating the parameters derived by the HAWC measurements to lower energies. As the positron excess primarily occurs between 10 GeV to 1 TeV, the GeV gamma-ray measurements of the Geminga halo would impose more direct constraints on the positron injection spectrum and the diffusion coefficient within this energy range [19, 58, 59]. However, there is no definitive conclusion on the GeV measurements of the Geminga halo at present.

VI. CONCLUSION

Based on the latest SBP and gamma-ray spectrum measurements of the Geminga halo by HAWC, we have studied the slow-diffusion zone size (r_*) around Geminga and the parameters of the electron injection spectrum. Current theories expect slow diffusion to be confined within tens of parsecs around Geminga, leading us to employ a two-zone diffusion model to characterize electron propagation. Our results suggest that r_* is within the range of 30 – 70 pc. The lower end of this range is constrained by the goodness of fit when fitting the SBP with the model. Models with $r_* \lesssim 30$ pc are disfavored by the chi-square test with a confidence level higher than 95%. The SBP derived from these models declines too quickly with increasing θ compared to the data, owing to a significant drop in the electron number density beyond r_* .

The upper limit of r_* is estimated by fitting the gamma-ray spectrum of the Geminga halo, along with the expectations for the power-law index (p) of the electron injection spectrum based on simulations and PWN observations, where $p \gtrsim 1$. Under the two-zone diffusion model, the derived r_* exhibits an inverse correlation with p when fitting the angle-integrated gamma spectrum within 10° around the pulsar. For $r_* \gtrsim 70$ pc, the upper limit of p at a 3σ confidence level falls below 1, implying that those models are disfavored.

Conversely, when r_* is set to its lower limit of 30 pc, we obtain the maximum p permitted by the HAWC spectrum measurement, with an upper limit of 2.17 at a 3σ confidence level. We also find that when $r_* = 30$ pc and $p = 2.17$, the positron flux generated by Geminga at Earth fits well with the positron spectrum measured by AMS-02 in the 50 – 500 GeV

range, in terms of both the spectral shape and the absolute flux. Notably, the upper limit of p coincides with that required to interpret the diffuse gamma-ray excess using gamma-ray pulsar halos, where $p \approx 2.2$ [26]. Besides, the cutoff energy of the electron injection spectrum is determined to be ≈ 100 TeV.

In interpreting the gamma-ray spectrum of the halo, the energy index of the diffusion coefficient (δ) also exhibits degeneracy with p and r_* . We have considered several typical values for δ (0, 1/3, and 1/2). The above upper limits for r_* and p are derived under the condition of $\delta = 0$. If δ increases, these constraints would be stricter. For example, when $\delta = 1/2$, the upper limit for p would decrease to 1.65. In the near future, the Large High Altitude Air Shower Observatory (LHAASO) is expected to provide energy-dependent morphology measurements for the Geminga halo, which could break the degeneracy among the parameters.

The recent H.E.S.S. measurement to the Geminga halo has revealed an unexpected soft gamma-ray spectrum in the 1 – 10 TeV range within a 1° radius from the pulsar [60]. This finding appears to be at odds with the results obtained by HAWC. The spectral features below 10 TeV need further verification through the forthcoming LHAASO result.

ACKNOWLEDGMENTS

The author would like to thank H. Zhou and R. Torres for sharing the energy range of the Geminga halo morphology measurements and the point spread function size of HAWC. This work is supported by the National Natural Science Foundation of China under Grants No. 12105292 and No. U2031110.

-
- [1] B. M. Gaensler and P. O. Slane, *Ann. Rev. Astron. Astrophys.* **44**, 17 (2006), arXiv:astro-ph/0601081.
 - [2] T. Sudoh, T. Linden, and J. F. Beacom, *Phys. Rev. D* **100**, 043016 (2019), arXiv:1902.08203 [astro-ph.HE].
 - [3] K. Fang, *Front. Astron. Space Sci.* **9**, 1022100 (2022), arXiv:2209.13294 [astro-ph.HE].
 - [4] R.-Y. Liu, *Int. J. Mod. Phys. A* **37**, 2230011 (2022), arXiv:2207.04011 [astro-ph.HE].

- [5] R. López-Coto, E. de Oña Wilhelmi, F. Aharonian, E. Amato, and J. Hinton, *Nature Astron.* **6**, 199 (2022), arXiv:2202.06899 [astro-ph.HE].
- [6] C. Evoli, T. Linden, and G. Morlino, *Phys. Rev. D* **98**, 063017 (2018), arXiv:1807.09263 [astro-ph.HE].
- [7] K. Fang, X.-J. Bi, and P.-F. Yin, *Mon. Not. Roy. Astron. Soc.* **488**, 4074 (2019), arXiv:1903.06421 [astro-ph.HE].
- [8] R.-Y. Liu, H. Yan, and H. Zhang, *Phys. Rev. Lett.* **123**, 221103 (2019), arXiv:1904.11536 [astro-ph.HE].
- [9] S.-H. Wang, K. Fang, X.-J. Bi, and P.-F. Yin, *Phys. Rev. D* **103**, 063035 (2021), arXiv:2101.01438 [astro-ph.HE].
- [10] K. Fang, S.-Q. Xi, and X.-J. Bi, *Phys. Rev. D* **104**, 103024 (2021), arXiv:2107.02140 [astro-ph.HE].
- [11] K. Fang and X.-J. Bi, *Phys. Rev. D* **105**, 103007 (2022), arXiv:2203.01546 [astro-ph.HE].
- [12] K. Fang, S.-Q. Xi, L.-Z. Bao, X.-J. Bi, and E.-S. Chen, *Phys. Rev. D* **106**, 123017 (2022), arXiv:2207.13533 [astro-ph.HE].
- [13] A. Abeysekara *et al.* (HAWC), *Science* **358**, 911 (2017), arXiv:1711.06223 [astro-ph.HE].
- [14] F. Aharonian *et al.* (LHAASO), *Phys. Rev. Lett.* **126**, 241103 (2021), arXiv:2106.09396 [astro-ph.HE].
- [15] A. Albert *et al.* (HAWC), *Astrophys. J. Lett.* **944**, L29 (2023), arXiv:2301.04646 [astro-ph.HE].
- [16] D. Hooper, I. Cholis, T. Linden, and K. Fang, *Phys. Rev. D* **96**, 103013 (2017), arXiv:1702.08436 [astro-ph.HE].
- [17] K. Fang, X.-J. Bi, P.-F. Yin, and Q. Yuan, *Astrophys. J.* **863**, 30 (2018), arXiv:1803.02640 [astro-ph.HE].
- [18] X. Tang and T. Piran, *Mon. Not. Roy. Astron. Soc.* **484**, 3491 (2019), arXiv:1808.02445 [astro-ph.HE].
- [19] S.-Q. Xi, R.-Y. Liu, Z.-Q. Huang, K. Fang, and X.-Y. Wang, *Astrophys. J.* **878**, 104 (2019), arXiv:1810.10928 [astro-ph.HE].
- [20] K. Fang, X.-J. Bi, and P.-F. Yin, *Astrophys. J.* **884**, 124 (2019), arXiv:1906.08542 [astro-ph.HE].
- [21] S. Manconi, M. Di Mauro, and F. Donato, *Phys. Rev. D* **102**, 023015 (2020), arXiv:2001.09985 [astro-ph.HE].

- [22] D. Wu, *JCAP* **12**, 007 (2022), arXiv:2206.07621 [astro-ph.HE].
- [23] B. Schroer, C. Evoli, and P. Blasi, *Phys. Rev. D* **107**, 123020 (2023), arXiv:2305.08019 [astro-ph.HE].
- [24] T. Linden and B. J. Buckman, *Phys. Rev. Lett.* **120**, 121101 (2018), arXiv:1707.01905 [astro-ph.HE].
- [25] A. Dekker, I. Holst, D. Hooper, G. Leone, E. Simon, and H. Xiao, (2023), arXiv:2306.00051 [astro-ph.HE].
- [26] K. Yan, R.-Y. Liu, R. Zhang, C.-M. Li, Q. Yuan, and X.-Y. Wang, (2023), arXiv:2307.12363 [astro-ph.HE].
- [27] P. Mukhopadhyay and T. Linden, *Phys. Rev. D* **105**, 123008 (2022), arXiv:2111.01143 [astro-ph.HE].
- [28] P. De La Torre Luque, O. Fornieri, and T. Linden, *Phys. Rev. D* **106**, 123033 (2022), arXiv:2205.08544 [astro-ph.HE].
- [29] K. Fang, H.-B. Hu, X.-J. Bi, and E.-S. Chen, *Phys. Rev. D* **108**, 023017 (2023), arXiv:2304.04570 [astro-ph.HE].
- [30] S. Recchia, M. Di Mauro, F. A. Aharonian, L. Orusa, F. Donato, S. Gabici, and S. Manconi, *Phys. Rev. D* **104**, 123017 (2021), arXiv:2106.02275 [astro-ph.HE].
- [31] L.-Z. Bao, K. Fang, X.-J. Bi, and S.-H. Wang, *Astrophys. J.* **936**, 183 (2022), arXiv:2107.07395 [astro-ph.HE].
- [32] A. Albert *et al.* (HAWC), *PoS ICRC2023*, 710 (2023).
- [33] B. B. Wang, G. P. Zank, L. L. Zhao, and L. Adhikari, *Astrophys. J.* **932**, 65 (2022).
- [34] J. Yao *et al.*, *Astrophys. J.* **939**, 75 (2022), arXiv:2209.14059 [astro-ph.HE].
- [35] Q. Yuan, S.-J. Lin, K. Fang, and X.-J. Bi, *Phys. Rev. D* **95**, 083007 (2017), arXiv:1701.06149 [astro-ph.HE].
- [36] K. Fang, X.-J. Bi, S.-J. Lin, and Q. Yuan, *Chin. Phys. Lett.* **38**, 039801 (2021), arXiv:2007.15601 [astro-ph.HE].
- [37] R. N. Manchester, G. B. Hobbs, A. Teoh, and M. Hobbs, *Astron. J.* **129**, 1993 (2005), arXiv:astro-ph/0412641.
- [38] P. Dempsey and P. Duffy, *Mon. Not. Roy. Astron. Soc.* **378**, 625 (2007), arXiv:0704.0168 [astro-ph].
- [39] S. M. Osipov, A. M. Bykov, A. E. Petrov, and V. I. Romansky, *J. Phys. Conf. Ser.* **1697**,

- 012009 (2020).
- [40] G. Blumenthal and R. Gould, *Rev. Mod. Phys.* **42**, 237 (1970).
 - [41] J. Faherty, F. M. Walter, and J. Anderson, *Astrophys. Space Sci.* **308**, 225 (2007).
 - [42] E.-S. Chen *et al.* (LHAASO), *PoS ICRC2023*, 613 (2023).
 - [43] P. Reichherzer, L. Merten, J. Dörner, J. Becker Tjus, M. J. Pueschel, and E. G. Zweibel, *Appl. Sciences* **4**, 15 (2022), arXiv:2104.13093 [astro-ph.HE].
 - [44] H. Yan and A. Lazarian, *Astrophys. J.* **673**, 942 (2008), arXiv:0710.2617 [astro-ph].
 - [45] A. M. Bykov, E. Amato, A. E. Petrov, A. M. Krassilchtchikov, and K. P. Levenfish, *Space Sci. Rev.* **207**, 235 (2017), arXiv:1705.00950 [astro-ph.HE].
 - [46] B. Posselt, G. Pavlov, P. Slane, R. Romani, N. Bucciantini, A. Bykov, O. Kargaltsev, M. Weiskopf, and C. Y. Ng, *Astrophys. J.* **835**, 66 (2017), arXiv:1611.03496 [astro-ph.HE].
 - [47] A. Khokhriakova, W. Becker, G. Ponti, M. Sasaki, B. Li, and R. Y. Liu, (2023), arXiv:2310.10454 [astro-ph.HE].
 - [48] O. Adriani *et al.* (PAMELA), *Nature* **458**, 607 (2009), arXiv:0810.4995 [astro-ph].
 - [49] M. Ackermann *et al.* (Fermi-LAT), *Phys. Rev. Lett.* **108**, 011103 (2012), arXiv:1109.0521 [astro-ph.HE].
 - [50] M. Aguilar *et al.* (AMS), *Phys. Rev. Lett.* **110**, 141102 (2013).
 - [51] D. Hooper, P. Blasi, and P. D. Serpico, *JCAP* **01**, 025 (2009), arXiv:0810.1527 [astro-ph].
 - [52] H. Yuksel, M. D. Kistler, and T. Stanev, *Phys. Rev. Lett.* **103**, 051101 (2009), arXiv:0810.2784 [astro-ph].
 - [53] P.-F. Yin, Z.-H. Yu, Q. Yuan, and X.-J. Bi, *Phys. Rev. D* **88**, 023001 (2013), arXiv:1304.4128 [astro-ph.HE].
 - [54] M. Aguilar *et al.* (AMS), *Phys. Rev. Lett.* **122**, 041102 (2019).
 - [55] A. Kounine, *PoS ICRC2023*, 065 (2023).
 - [56] A. M. Bykov, A. E. Petrov, A. M. Krassilchtchikov, K. P. Levenfish, S. M. Osipov, and G. G. Pavlov, *Astrophys. J. Lett.* **876**, L8 (2019), arXiv:1904.09430 [astro-ph.HE].
 - [57] P. Martin, A. Marcowith, and L. Tibaldo, *Astron. Astrophys.* **665**, A132 (2022), arXiv:2206.11803 [astro-ph.HE].
 - [58] M. Di Mauro, S. Manconi, and F. Donato, *Phys. Rev. D* **100**, 123015 (2019), [Erratum: *Phys.Rev.D* 104, 089903 (2021)], arXiv:1903.05647 [astro-ph.HE].
 - [59] G.-Y. Zhou, Z.-H. Yu, Q. Yuan, and H.-H. Zhang, *Commun. Theor. Phys.* **74**, 105403 (2022),

arXiv:2205.07038 [astro-ph.HE].

- [60] F. Aharonian *et al.* (H.E.S.S.), *Astron. Astrophys.* **673**, A148 (2023), arXiv:2304.02631 [astro-ph.HE].